International Journal of Microwave and Wireless Technologies

cambridge.org/mrf

Broadband packaging solution in embedded wafer level ball grid array technology for D-band PMCW radar

Elizabeth Bekker, Georg Gramlich, Luca Valenziano, Lucas Giroto de Oliveira, Theresa Antes, Thomas Zwick and Akanksha Bhutani

Institute of Radio Frequency Engineering and Electronics, Karlsruhe Institute of Technology, Karlsruhe, Germany

Research Paper

Cite this article: Bekker E, Gramlich G, Valenziano L, de Oliveira LG, Antes T, Zwick T, Bhutani A (2024) Broadband packaging solution in embedded wafer level ball grid array technology for D-band PMCW radar. *International Journal of Microwave and Wireless Technologies* **16**(5), 771–782. https://doi.org/10.1017/S1759078724000266

Received: 23 June 2023
Revised: 30 January 2024
Accepted: 1 February 2024

Keywords:
antennas and packaging; embedded wafer level ball grid array (eWLB); millimeter wave radar

Corresponding author: Elizabeth Bekker;
Email: elizabeth.bekker@kit.edu

Abstract

A system-in-package for a wideband digital radar, in D-band, requires broadband, high-gain antennas combined with broadband chip-to-package and package-to-printed circuit board (PCB) interconnects. This paper demonstrates a wideband, low-loss quasi-coaxial signal transition, and a novel electric split ring resonator (eSRR)-based antenna-in-package (AiP) with a modified reflector concept, for improved gain, in embedded wafer level ball grid array (eWLB) technology. A complete chip-to-package-to-PCB interconnect is also demonstrated by combining the quasi-coaxial transition with a chip-to-package interconnect. The quasi-coaxial signal transition has the largest impedance bandwidth among ball grid array-based quasi-coaxial signal transitions. For the modified reflector concept, a horn-shaped cavity is micromachined in the PCB substrate and remetallized with aerosol-jet printing, placing the reflector 0.25λ from the antenna. The antenna gain is improved with up to 5.3 dB. The AiP with the horn-shaped reflector is the single element with the highest gain, in eWLB technology, above 100 GHz.

Introduction

Recently, there has been a drive to release additional parts of the spectrum above 116 GHz for novel sensing applications [1]. With the large amount of bandwidth available at these frequencies, such as in D-band for instance, radars with an ever greater range resolution is achievable and due to the short wavelength, the radar can be very compact. This makes it easy to integrate the sensor into different devices for a new generation of touchless, intuitive human–machine interactions. In this context, the components detailed in this work have been tailored for a broadband, 140 GHz radar transceiver. While their application is versatile, the specific motivation behind their development centered on their integration with a 140 GHz phase-modulated continuous wave (PMCW) radar, designed to offer a 12.5 GHz baseband bandwidth, specifically for hand gesture recognition [2, 3].

Naturally, radar sensors for hand gesture recognition, at such frequencies, are not without their challenges. Constraints on transmitter power, receiver sensitivity, and significant free space path loss at 140 GHz are among these obstacles. The nature of the target, a moving hand performing complex gestures, also dictates certain system requirements. To compound the problem, it has been determined that the radar cross-section of a human hand can be as low as −45 dBsm [4], although it depends on the gesture. These challenges necessitate antennas with sufficiently high gain.

Excellent range resolution is also required to be able to distinguish between small targets. In radar systems, the range resolution improves with an increase in the bandwidth. In PMCW radar specifically, the bandwidth is directly proportional to the sampling rate of the chosen pseudorandom binary sequence [5]. Elevated sampling frequencies, necessitates a higher clock frequency and an increased analog-to-digital converter output sampling rate. Therefore, for fine range resolutions, the interconnect between the packaged transceiver and the field programmable gate array (FPGA) will require an expansive bandwidth. Additionally, for the aforementioned PMCW radar, the voltage-controlled oscillator (VCO) will be off-chip, residing on the printed circuit board (PCB). Positioning the VCO on the PCB enables the use of standard, off-the-shelf VCOs typically having higher output power. A high-power VCO greatly enhances the signal-to-noise ratio. Heat management is also more straightforward on the PCB, through the use of large heat sinks. For the D-band radar discussed above, the VCO operates at 35 GHz; thus, future radar applications at higher frequencies will require proportionally higher VCO frequencies.

© The Author(s), 2024. Published by Cambridge University Press in association with The European Microwave Association. This is an Open Access article, distributed under the terms of the Creative Commons Attribution licence (http://creativecommons.org/licenses/by/4.0), which permits unrestricted re-use, distribution and reproduction, provided the original article is properly cited.

CAMBRIDGE UNIVERSITY PRESS

Therefore, one can conclude, high-gain, broadband antennas combined with broadband chip-to-package and package-to-printed circuit board (PCB) interconnects are required for PMCW radars with a high sampling rate. This work presents a broadband packaging solution within the D-band, using embedded wafer level ball grid array (eWLB) technology. Two crucial components required for a wideband system-in-package (SiP) are demonstrated for the first time in eWLB technology: a wideband, low-loss quasi-coaxial signal transition, and an innovative electric split ring resonator (eSRR)-based antenna-in-package (AiP) featuring an enhanced reflector design for superior gain. Subsequent sections provide a concise overview and comparison with contemporary eWLB antennas and ball grid array (BGA)-based quasi-coaxial interconnects.

AiP in eWLB

Embedded wafer level ball grid array (eWLB) technology is a favorable packaging technology for millimeter-wave systems due to a variety of reasons [6]. A key advantage is the minimization of package loss due to compact microvias forming the monolithic microwave integrated circuit (MMIC)-to-package interconnects, and the mold compound exhibiting a stable dielectric constant and a low loss tangent, above 100 GHz. Additionally, antennas and signal lines can be realized in a redistribution layer (RDL) with excellent precision and resolution. Figure 1(a) shows a simplified cross-section of a standard eWLB package.

Several antennas have been realized in eWLB at 60 GHz [7] and 77 GHz [8, 9]. However, designs beyond 100 GHz are limited. The 120 GHz differential bow-tie and a 240 GHz single-ended slot-type bow-tie from [10] are of note. To date, the antennas in [10] have the highest bandwidth of eWLB antennas, above 100 GHz. Regarding wideband antennas centered around 140 GHz, a single-ended corner patch element from [11] and results for a dipole, bow-tie, and rhombic differential antenna [12] have been published. The round SRR antenna from [13] and the differential, square SRR (SSRR) antenna from [14] are significant contributions in this area. The SSRR had the highest gain, for a single antenna element, in eWLB packaging technology, above 100 GHz, to date. The work presented here is an extension of work first presented in [14].

Despite the fact that the reflector on the PCB has a significant impact on the antenna gain in an eWLB package, possible improvements related to the reflector, remain unexplored. Typically, a planar reflector, placed 0.1λ (at 140 GHz) from the antenna, is used. This antenna-to-reflector distance is fixed by the size of the solder balls used in a BGA and the parameters used in a reflow soldering process. This work introduces a differential electric SRR (eSRR) antenna with augmented gain via a cavity micro-machined and re-metallized in the PCB substrate. The horn-shaped reflector is set at a $\lambda/4$ distance from the eWLB antenna. The horn-shaped reflector concept, combined with an eWLB AiP, is shown in Fig. 1(b). To the best of the authors' knowledge, a differential eSRR AiP, with a horn-shaped reflector, which improves the peak gain by roughly 2.3 dB, is demonstrated here for the first time. The modified package concept results in a single antenna element with a peak gain surpassing that of [14], and is thus the highest to date.

BGA-based quasi-coaxial interconnects

Several published works have explored BGA-based quasi-coaxial interconnects. Shao et al. [15] introduced a broadband transition between a substrate integrated coaxial line (SICL) in low temperature co-fired ceramic (LTCC) technology, and BGA-based interconnect quasi-coaxial interconnect. The insertion and return loss results for the full back-to-back transition is obtained with a hybrid model, by cascading the measured SICL component, with the simulated parameters of the BGA transition. The tin BGA balls are assumed to have a diameter of 400 μm and height of only 100 μm. A DC to 35 GHz broadband interconnect in high temperature co-fired ceramic (HTCC) technology is presented in [16]. The structure connects two transmission line sections in HTCC, via a BGA-based quasi-coaxial transition. Likewise, in [17], a quasi-coaxial transition between two composite boards is realized in BGA. A coaxial BGA layout is also demonstrated in [18], to connect a HTCC substrate to a PCB for a broadband RF multi-chip SiP packaging module. In [19], a vertical quasi-coaxial interconnect connects two substrates, for use in 3-D SiP modules, at 60 GHz. The interconnect uses copper balls with a diameter of 350 μm, attached with solder paste to the upper and lower substrates. The single copper ball for the signal line is surrounded by six copper balls, forming the ground connection. A back-to-back prototype with CPW feed lines on the lower substrate and a CPW through line on the upper substrate, was manufactured. The quasi-coaxial interconnect in [19] is improved in [20], by forming an excavated structure to minimize fluctuation in the positions of the copper balls during the reflow process. A complex structure consisting of a stacked strip-line-to-quasi-coax and quasi-coax-to-GCPW transition, connecting 3 multi-layered substrates is shown and fabricated. In [21], a vertical quasi-coaxial connection is used to connect a chip to an external V-band waveguide through a fenced stripline in a multi-layer LTCC package. The flip chip bumps have a diameter of only 75 μm.

A wideband 140 GHz PMCW radar SiP necessitates broadband interconnects from chip-to-package and package-to-PCB. In this paper, a DC to 100 GHz quasi-coaxial signal transition is demonstrated in eWLB technology for the first time. The quasi-coaxial transition presented here has a return loss of greater than 10 dB, up to 103 GHz. Its insertion loss is less than 0.6 dB per transition, up to 80 GHz, and less than 2.2 dB, up to 100 GHz. From the excellent measured return loss and insertion loss values, one can conclude, a 50 Ω impedance is maintained as closely as possible throughout the chip-to-package-to-PCB interconnect. To the best of the

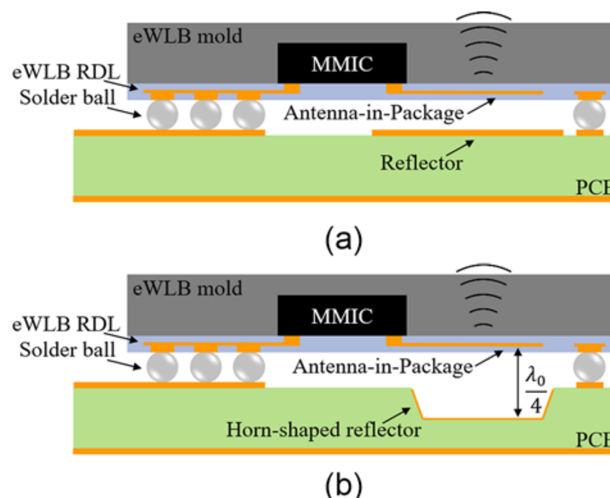

Figure 1. Simplified schematic of the cross-section of an eWLB package: (a) standard and (b) with a horn-shaped reflector.

https://doi.org/10.1017/S1759078724000266 Published online by Cambridge University Press

authors' knowledge, this eWLB-based quasi-coaxial signal transition exhibits the largest impedance bandwidth compared to the various published BGA-based quasi-coaxial interconnects, without requiring a special manufacturing technology (see Table 2). For context, the upper cutoff frequency for a 1 mm air coaxial connector, operating in its fundamental transverse electromagnetic (TEM) mode, is roughly 130 GHz, and these connectors are used up to 110 GHz. The quasi-coaxial signal transition demonstrated in this work closely approaches this limit, while considering eWLB manufacturing constraints. A full chip-to-package-to-PCB interconnect is also shown, in which the eWLB-based quasi-coaxial signal transition forms the package-to-PCB interconnect, and an on-chip through-line fabricated in 22-nm fully depleted silicon on insulator (FDSOI) CMOS technology is used to form the chip-to-package interconnect. These interconnects are realized in a back-to-back or daisy chain configuration, which enables probe-based S-parameter measurement.

The remainder of the paper is structured as follows. Section "Design" provides details on the design of the quasi-coaxial signal transition, the eSRR antenna and its horn-shaped reflector. In the "Manufacturing and assembly" section, the manufacturing of the horn-shaped reflector and the assembly of the packages are discussed. The results are presented in "Results" section, and the paper is concluded in last section.

Design

In this section, the design of the quasi-coaxial signal transition will be discussed first, followed by the design of the eSRR antenna and the horn-shaped reflector.

Chip-to-package-to-PCB interconnect

Three different interconnect structures are demonstrated in this paper, namely, a chip-to-package, a package-to-PCB and a chip-to-package-to-PCB interconnect. All interconnects are demonstrated in a daisy chain/back-to-back configuration to enable probe-based S-parameter measurement.

A chip-to-package interconnect realized by means of eWLB microvias is shown in Fig. 2(a). The design consists of ground plane taper connecting the RF pads on the chip, with a pitch of 125 μm, to the 50Ω CPW line in the RDL layer of an eWLB package. The on-chip through-line is fabricated in 22-nm FDSOI CMOS technology.

The package-to-PCB interconnect, realized by means of a quasi-coaxial signal transition (see Fig. 2(b)), is designed as follows. The first step in the design of the quasi-coaxial signal transition is to calculate the theoretical characteristic impedance of the quasi-coaxial signal transition, with the following equation from [22], for the impedance of a coaxial transmission line:

$$Z_{\text{coaxial}} = \frac{60}{\sqrt{\epsilon_r}} \ln\left(\frac{r_{\text{outer}}}{r_{\text{inner}}}\right). \tag{1}$$

As the BGA-based quasi-coaxial signal transition is air-filled, $\epsilon_r = 1$. The solder balls of the packages demonstrated in this paper in eWLB technology, have a standard pitch of 500 μm and diameter of 375 μm – see [6, 23]. This leads to an initial calculation of $Z_{\text{coaxial}} = 31\,\Omega$ for the quasi-coaxial signal transition. The quasi-coaxial transition supports the TEM mode. The cut-off frequency

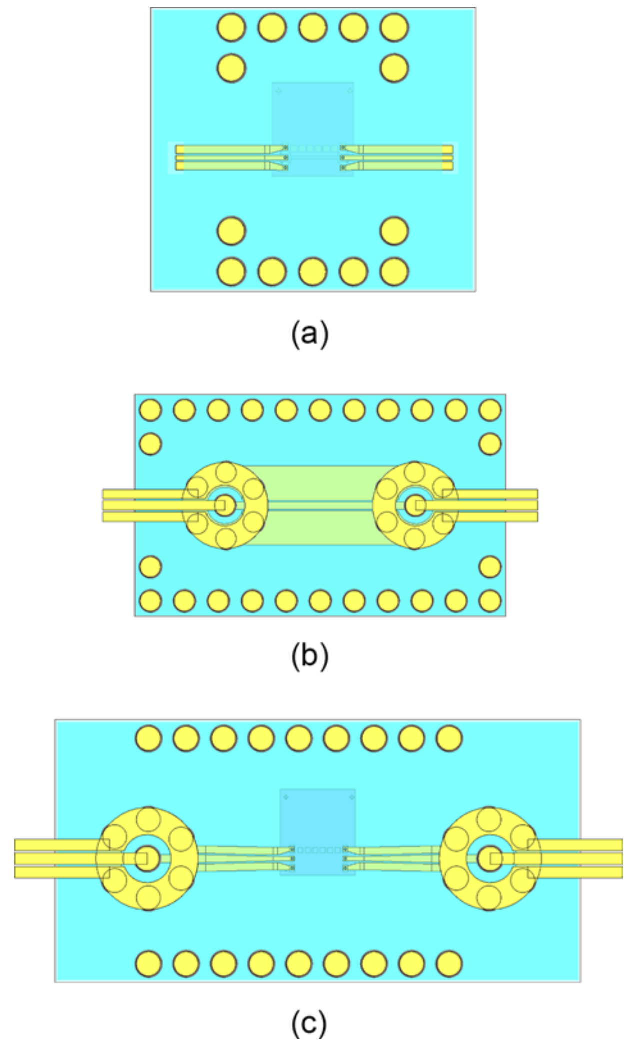

Figure 2. Interconnect design (shown without PCB substrate): (a) chip-to-package; (b) package-to-PCB; and (c) complete chip-to-package-to-PCB.

of the TE_{11} mode of a standard coaxial transmission line can be estimated with the following equation,

$$f_{\text{TE}_{11}} = \frac{c}{\pi\sqrt{\epsilon_r}(r_{\text{outer}} + r_{\text{inner}})}. \tag{2}$$

The cut-off frequency, for the initial design values mentioned above, is $f_{\text{TE}_{11}} = 139$ GHz, if one assumes r_{outer} to be defined as the pitch of the solder balls. This is more than sufficient for the proposed PMCW radar SiP application.

The position of the solder balls, the size of the ground ring on the package and on the PCB, as well as the width of the finite ground plane in the package, is subsequently optimized in CST Studio Suite software – taking into consideration, the design rules of the eWLB manufacturing technology. The simulation model for the optimization process can be seen in Fig. 3(a) – two waveguide ports are placed on either side of the quasi-coaxial signal transition. The insertion and return loss for the optimized signal transition model is given in Fig. 3(b). The characteristic impedance of the optimized quasi-coaxial signal transition is calculated with [24]:

$$Z_c = Z_0\sqrt{\frac{(1+S_{11})^2 - S_{21}^2}{(1-S_{11})^2 - S_{21}^2}}. \tag{3}$$

https://doi.org/10.1017/S1759078724000266 Published online by Cambridge University Press

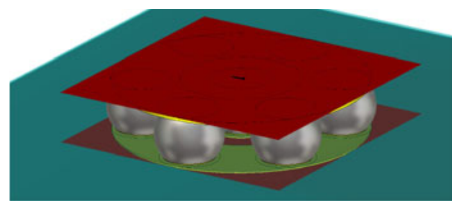

(a)

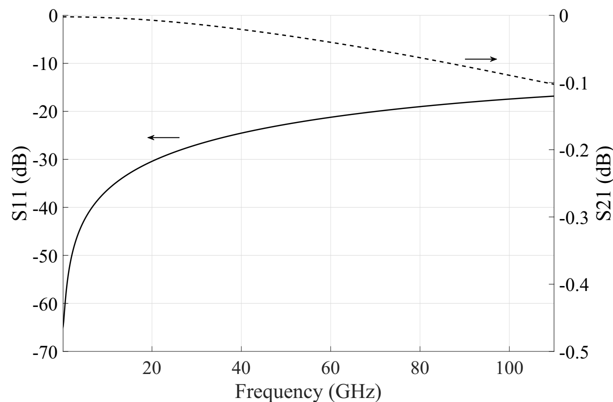

(b)

Figure 3. Quasi-coaxial signal transition: (a) simulation model for optimization and (b) simulation results.

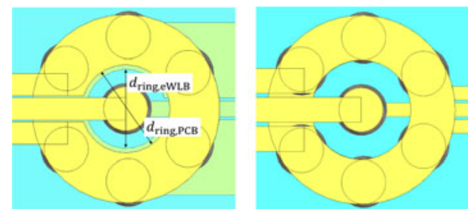

(a) (b)

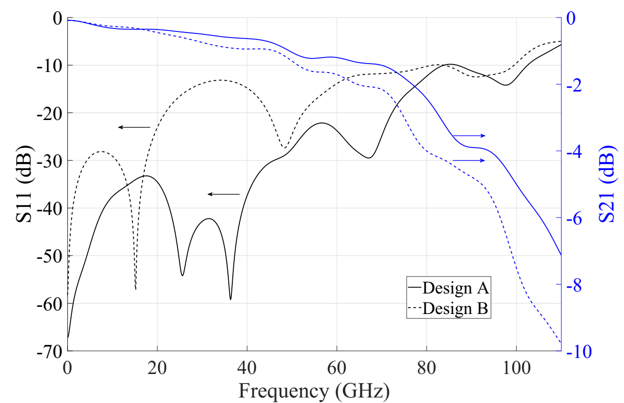

(c)

Figure 4. Two models of the quasi-coaxial signal transition: (a) Design A; (b) Design B; and (c) comparison of results.

Using Eq. (3), the characteristic impedance is calculated as 40.3 Ω, at a center frequency of 55 GHz. Thereafter, the quasi-coaxial signal transition is connected to 50 Ω CPW lines on the package and PCB.

Two models for the quasi-coaxial signal transition are presented here – Design A (Fig. 4(a)) and Design B (Fig. 4(b)). Design A has been optimized to ensure minimal return and insertion losses over an expansive bandwidth. Contrarily, Design A is characterized by an extended ground plane and reduced inner ground ring diameter compared to Design B, with $d_{\text{ring, eWLB}} = 0.576$ mm, $d_{\text{ring, PCB}} = 0.64$ mm. Design B boasts a more compact footprint, but it incurs a marginally higher insertion loss in comparison with Design A. Design B has a more compact footprint, with narrower ground planes, but it incurs a marginally higher insertion loss in comparison with Design A. The inner diameter of the ground ring on the package is also larger for Design B – $d_{\text{ring, eWLB}} = d_{\text{ring, PCB}} = 0.72$ mm. Furthermore, Design B seamlessly integrates with the chip-to-package interconnect presented earlier. Nonetheless, both Designs A and B of the quasi-coaxial signal transition remain viable options; using Design A would merely necessitate adjusting the chip-to-package interconnect to accommodate the broader ground plane. The return and insertion loss of the back-to-back quasi-coaxial-to-CPW signal transition, with a CPW line 1.65 mm long connecting the two quasi-coaxial transitions, are shown in Fig. 4(c), for both designs. A back-to-back model of Design A of the quasi-coaxial signal transition is manufactured, to illustrate the wideband characteristics of the eWLB-based quasi-coaxial signal transition for the first time.

Lastly, the quasi-coaxial signal transition given in Fig. 4(b) (Design B) is used in the design of the full back-to-back chip-to-package-to-PCB interconnect – see Fig. 2(c) – due to ease of integration and the smaller area requirement. All the interconnects presented in this section use RO4003C, with a thickness of 508 μm as PCB substrate.

eSRR antenna

The design of the eSRR antenna is based on electrically resonant terahertz metamaterial unit cells originally proposed in [25, 26]. Unlike classic SRRs, whose electric and magnetic responses are strongly coupled (resulting in a complex magnetoelectric response), eSRRs have a pure electric response [25]. The symmetrical structure of an eSRR eliminates the magnetoelectric response by counter-circulating currents in the unit cell. Figure 5 shows the design and dimensions of the novel, uniaxial, differential eSRR antenna, that is demonstrated in this paper for the first time. The width of the strip closest to the feed was increased to improve the matching and return loss. The antenna is square, with $l_1 = 0.27\lambda_g$ (λ_g is the guided wavelength) and when including the surrounding finite ground conductor, $l_2 = 0.48\lambda_g$. The antenna is realized in an eWLB package of 4×5 mm^2.

The antenna has a 100 Ω coplanar strip line (CPS) for its feed. A probe-based antenna measurement setup is used [27] to characterize D-band antennas from 110 to 170 GHz. For D-band measurements, single-ended probes are used, therefore, a balanced-to-unbalanced (i.e. balun) transition is required when measuring differential antennas. A Chebyshev quarter-wave stepped balun transformer is used for the 50 Ω CPW to 100 Ω CPS transition – previously characterized in [12]. This balun necessitates bond wires to bridge the finite ground planes. The bond wires are added manually during the assembly process. Two bond wires are added on both sides of the radial slot. The balun's intended application is solely for the antenna characterization, and considering that MMICs frequently adopt differential outputs, it is

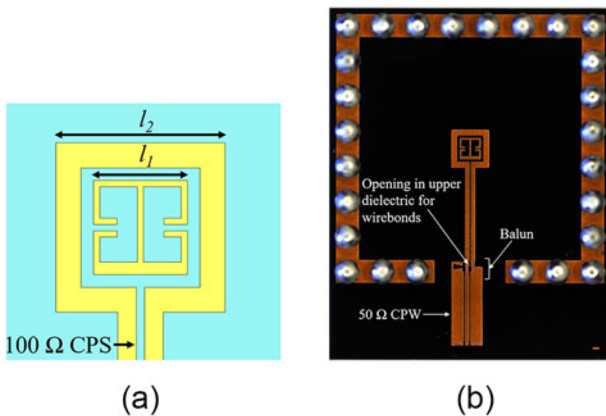

Figure 5. eSRR antenna: (a) simulation model with dimensions and (b) microscope photo of a prototype.

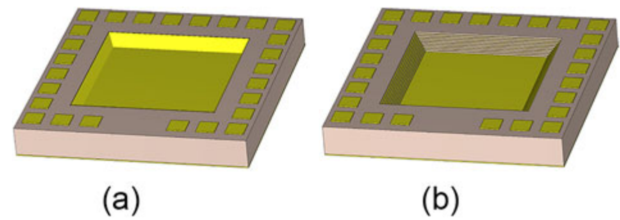

Figure 6. Simulation models of horn-shaped reflector of eSRR antenna: (a) simplified model of smooth horn and (b) horn shape approximated by metallized steps.

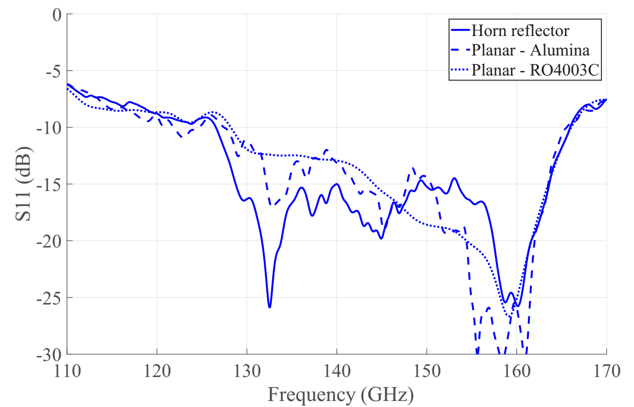

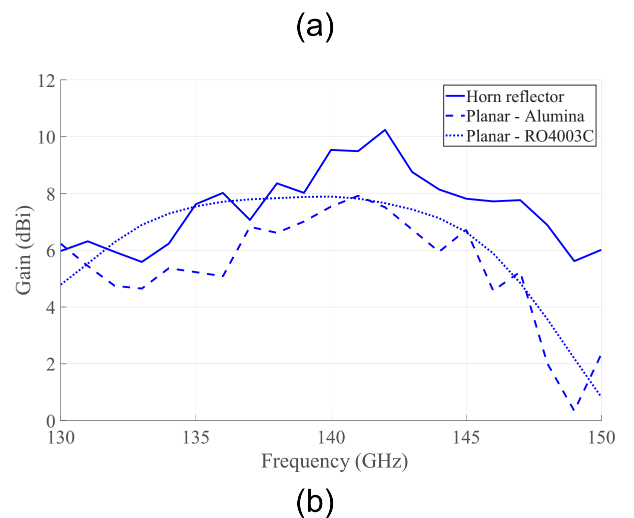

Figure 7. Simulation results of eSRR antenna with different reflectors: (a) reflection coefficient and (b) antenna gain.

not intended for integration into future products. A microscope photo of the differential eSRR antenna prototype, with the aforementioned Chebyshev balun, in the eWLB package, is shown in Fig. 5.

As can be seen from Fig. 1(a), the antenna's radiation is reflected by the reflector realized on the PCB and therefore radiates through the mold, in the direction opposite of the feedline and probe. In this paper, a simple change is introduced in the conventional eWLB-package-and-PCB assembly, which enhances the gain of an eWLB AiP significantly. Due to the height of the solderballs after soldering and assembly, the usual distance between the antenna and reflector, is approximately 0.1λ, at 140 GHz. By simply increasing the distance between the eWLB AiP and a PCB-based reflector, to 0.25λ, constructive interference of the electric fields should result in a higher antenna gain. Therefore, 290 μm is additionally required between the antenna and the reflector – this is used as the initial value for the depth of the horn-shaped reflector. This idea leads to the proposed modified package concept illustrated in Fig. 1(b), where a horn-shaped reflector is manufactured in the PCB, instead of a planar reflector as was custom in previous publications [11]–[14].

Of course, a smooth horn is difficult to realize in alumina substrate. The horn ramp is approximated with steps of 20 μm – see Fig. 6(b). A VBA macro is used to model the layers in CST. It was determined in simulation that as long as the steps are less than 25 μm in height, the AiP performance is similar to that of the simulation model using a smooth horn (Fig. 6(a)). It is further determined, through optimization in CST Studio Suite software, that a slope of 15°, and a horn aperture of 2.5×2.5 mm^2 results in an optimum gain value, and a horn height of 260 μm leads to the highest average gain from 130 to 150 GHz. The total substrate thickness of the alumina in which the horn-shaped reflector is realized, is 508 μm – a standard sheet thickness.

In Fig. 7, the return loss and the gain of the eSRR antenna, with three different reflectors, are presented – two planar reflectors and the horn-shaped reflector described above. The results for two different planar reflectors are presented – for an antenna with a Rogers 4003C substrate and an alumina substrate. In both cases, the PCB substrate is 508 μm thick with a 2.25×2.25 mm^2 reflector on the PCB. The RO4003C simulation results are included here, to ease comparison with prior works [11]–[14] that used a similar substrate. The impedance bandwidth of the three different scenarios are similar – the reflection coefficient is below −10 dB from 127 to 166 GHz (a relative bandwdith of 26.9%). The gain, however, improves quite significantly, with the antenna with the horn-shaped reflector exhibiting a peak gain of 10.2 dBi – an improvement of 2.3 dB from the case of the planar reflector. A significant improvement is especially noticeable at the higher frequencies – an improvement of up to 5.3 dB can be seen around 149 GHz.

Manufacturing and assembly

The eWLB packages of the antenna and interconnect prototypes are manufactured by Infineon AG. Microscope photos of the manufactured prototypes of the interconnects can be seen in Figs. 8(a),

https://doi.org/10.1017/S1759078724000266 Published online by Cambridge University Press

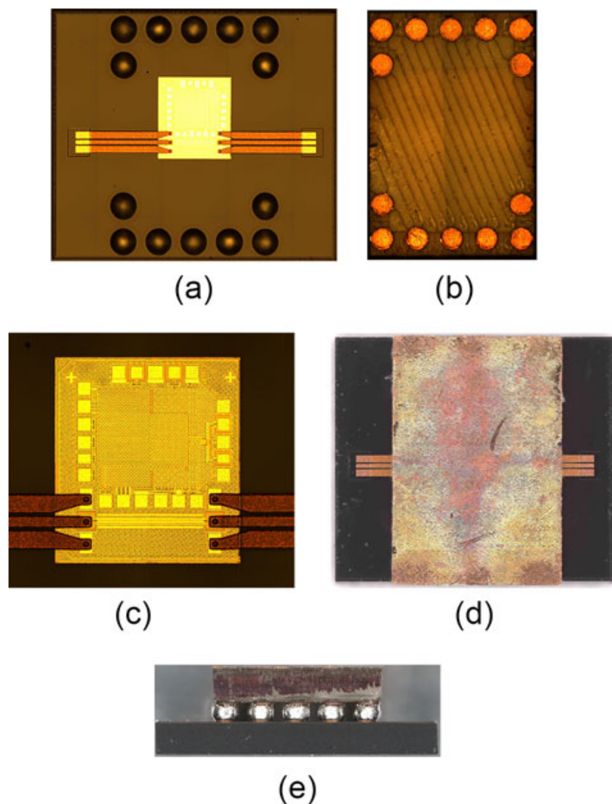

Figure 8. Chip-to-package interconnect: (a) eWLB package; (b) PCB; (c) transition and MMIC details; (d) top view of assembled package; and (e) side view of assembled package.

9(a) and 10(a). The antenna prototype can be seen in Fig. 5(b). The fabrication and assembly of the eWLB AiP presented in this paper requires four additional key steps. The first is the structuring of the alumina substrate, the second one is re-metallizing the reflector using aerosol-jet printing, the third step is connecting the ground planes of the balun with bondwires, and the final step is the assembly of the package and the reflector. For the interconnects, the PCBs are manufactured through laser ablation as well, and subsequently soldered onto the package. The manufacturing and assembly steps are described in more detail in the following section.

Laser-structuring

The laser used in this work is the ProtoLaser R4 by LPKF – it is a green picosecond laser for cold ablation with a spot size of 20 μm. It can structure a wide range of materials including widely used PCB materials such as the gold-coated alumina or copper-plated RO4003C used in this work. For the interconnects, one side of the RO4003C substrate is structured using this laser – see Figs. 8(b), 9(b) and 10(b) for microscope photos of the PCB prototypes. As for the PCB-based reflector, a more involved process is required. A customized process is developed to manufacture the horn-shaped cavity for the antenna reflector, as the machine does not come with such a ready-to-use functionality. As a first step, a simple cavity in alumina is manufactured, and its depth measured. Knowing the depth and the number of hatching repetitions necessary to make the simple cavity allows one to determine the ablation height per repetition. In the next step, the number of repetitions per layer are chosen, so that it would cut 25 μm deep per layer, and

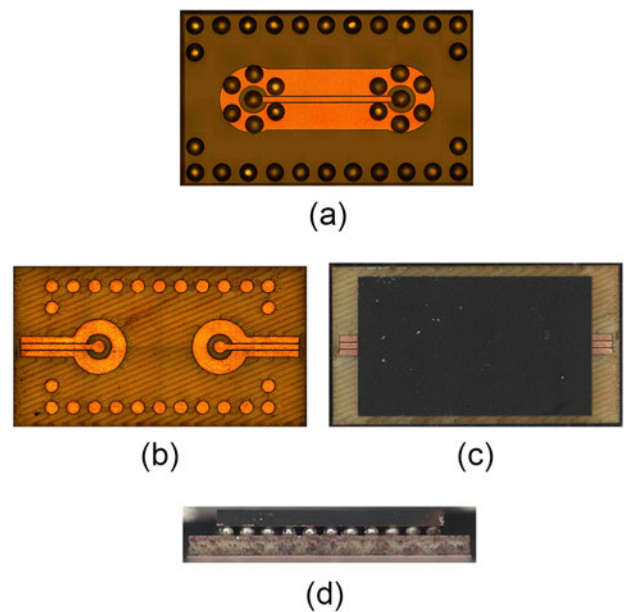

Figure 9. Package-to-PCB interconnect based on quasi-coaxial signal transition: (a) eWLB package; (b) PCB; (c) top view of assembled package; and (d) side view of assembled package.

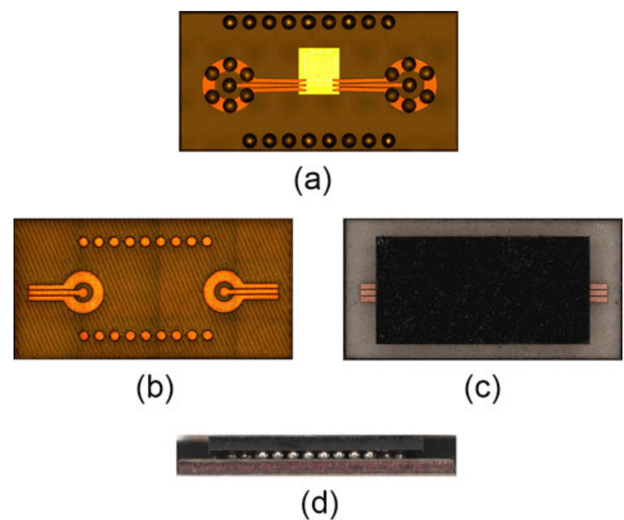

Figure 10. Complete chip-to-package-to-PCB chain with quasi-coaxial interconnect: (a) eWLB package; (b) PCB; (c) top view of assembled sample; and (d) side view of assembled sample.

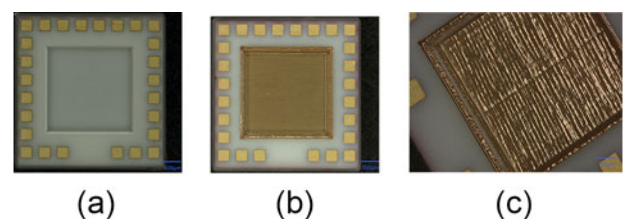

Figure 11. Manufactured prototype of horn-shaped reflector of eSRR antenna: (a) prior to metallization; (b) after metallization with AJ-printing; and (c) step with missing metallization.

thereafter a set of layers with decreasing cavity dimensions, is created. Controlling the difference in size between the layers means

https://doi.org/10.1017/S1759078724000266 Published online by Cambridge University Press

controlling the horn slope. A microscope photo of the horn-shaped cavity in the alumina can be seen in Fig. 11(a).

Aerosol-jet printing

Aerosol-jet (AJ) printing is a non-contact printing process, that can create feature sizes down to 10 μm and use a wide range of materials – including silver. The working principle is described in [28]. This work required plating the walls and bottom of the previously manufactured horn-shaped reflector. A 100 μm nozzle is the best suited for these constraints. All printing parameters are given in Table 1. The AJ5X printer by Optomec is used here, in a cleanroom environment, and 3-min oxygen plasma pretreatment was applied to the substrates. Thereafter, they were sintered for 5 min on a preheated hotplate at 250 °C. A microscopic image of the metallized horn is shown in Fig. 11(b). In order to obtain a continuous metal layer, an additional deposition step was added on the slopes. As the slope of the cavity is quite steep, some steps might not be metallized – this can be seen in the photo of Fig. 11(c).

Table 1. Aerosol jet printing parameters

Sheath	Atomizer	UA power	UA temp.
25 SCCM	13 SCCM	500 mA	24 °C
Platen temp.	Printing speed	Line width	Line pitch
25 °C	2 mm/s	28 μm	18 μm

Wire bonding and assembly

As mentioned above, two bond wires are added on both sides of the radial slot. An opening was left in the upper dielectric layer of the eWLB package, in the region of the balun, to expose the copper RDL layer. The dielectric opening is only 220 μm × 160 μm. The bond wires are made from gold wire with a diameter of 17.5 μm. As such it is quite challenging to fit all four, such short, bond wires in the limited dielectric opening, without accidentally shorting the signal line. A tungsten wire with a diameter of 50 μm was held in place on the signal line to prevent causing a short

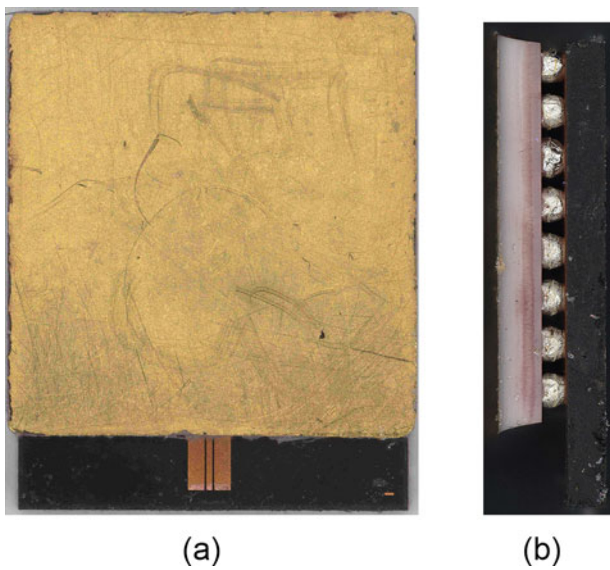

Figure 12. Microscope photo of prototype of eSRR antenna with horn-shaped reflector: (a) top view and (b) side view.

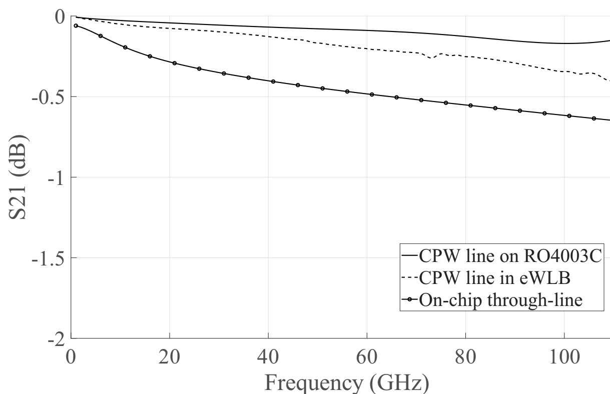

Figure 13. Simulated insertion loss of a CPW line on PCB, a CPW line in eWLB technology and the on-chip microstrip line.

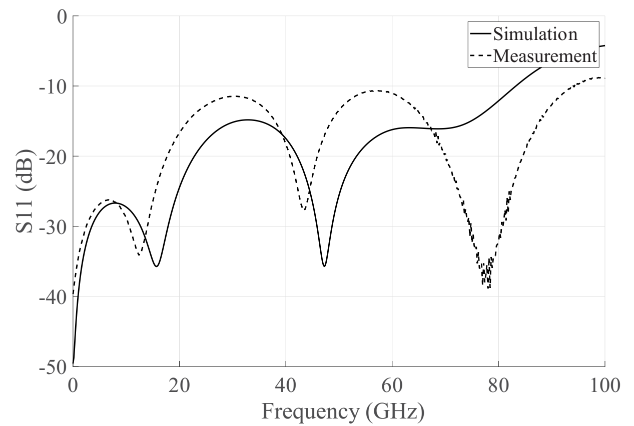

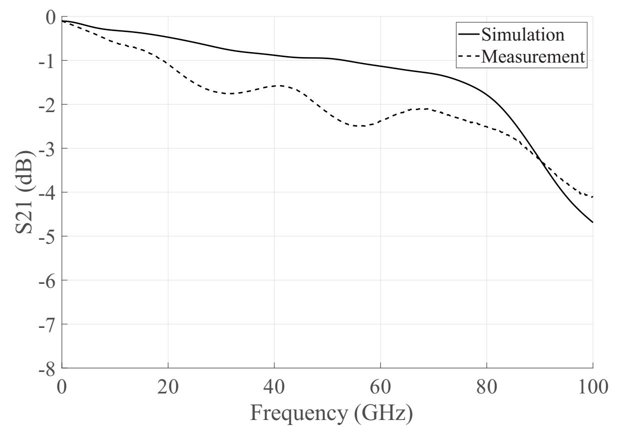

Figure 14. Measurement and simulation results of chip-to-package interconnect: (a) return loss and (b) insertion loss.

https://doi.org/10.1017/S1759078724000266 Published online by Cambridge University Press

circuit with the signal line and to ensure that the final height of the bond wires were approximately 50 μm. The F&S Bondtec Series 56i wire bonder was used. The eWLB packages are manually soldered to the laser-structured PCBs, using the Finetech Fineplacer Lambda. Microscope photos of the assembled packages can be seen in Figs. 8(d, e), 9(c, d), 10(c, d), and 12.

Results

The simulation and measurement results for the interconnects are discussed first, after which the results for the high gain eSRR-based antenna are presented.

Chip-to-package-to-PCB interconnect

In this section, the results for each of the back-to-back interconnect structures are discussed. In order to calculate the loss for the interconnects or transitions, it is necessary to know the insertion loss of a 50 Ω CPW line on the RO4003C PCB substrate, a 50 Ω CPW line realized in the RDL layer of an eWLB package and that of the on-chip microstrip line. The simulation results for the insertion loss of these structures are shown Fig. 13. The CPW lines are both 1 mm in length and the on-chip through-line is 0.58 mm in length.

The simulation and measurement results of the chip-to-package interconnect, shown in Fig. 8, can be found in Fig. 14. Overall, the measured and simulated results agree well. The insertion loss is less than 3 dB up to 88 GHz, for both the simulation and measurement. The return loss is greater than 10 dB up to 83 GHz, for the simulated case, and greater than 10 dB up to 94 GHz, for the measurement. The total length of the CPW line in the RDL layer of the package shown in Fig. 8, was 2.2 mm. From Fig. 13, a loss of approximately 0.17 dB/mm can be expected at 50 GHz. Therefore, 0.44 dB loss can be attributed to the CPW line in the package. Similarly, at 50 GHz, the on-chip transmission line has an insertion loss of 0.45 dB. The measured insertion loss of the back-to-back chip-to-package structure is 2.2 dB at 50 GHz – see Fig. 14. Therefore, the insertion loss per transition (including the chip pads, eWLB microvias and the taper) would be approximately 0.7 dB. The stackup of the on-chip structures manufactured in the 22 nm FDSOI CMOS technology has to be simplified, in order to simulate the detailed interconnect in a reasonable computation time. The difference between the simulation and measurement results can partly be attributed to this simplification of the on-chip structures. The differences can also stem from calibration or measurement errors, or a shift between the RDL and the chip during the overmolding process, causing a rotation or a shift in the x- or y-directions. Furthermore, the decline after 80 GHz can be due to the parasitics stemming from the overlap between the interconnect and the chip pads, as well as the parasitics of the chip pads themselves.

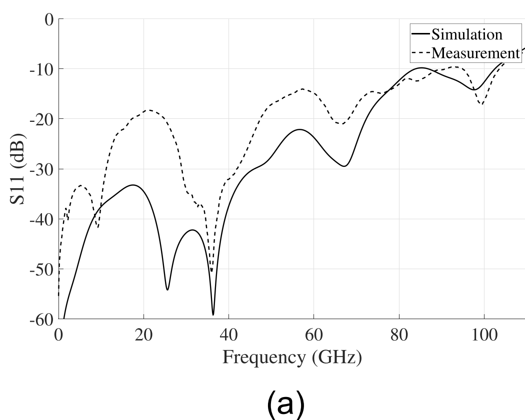

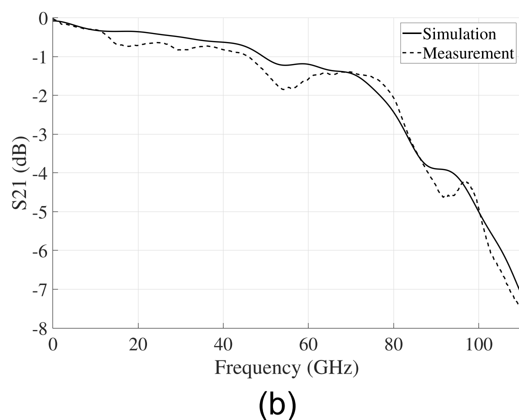

Figure 15. Measurement and simulation results of package-to-PCB interconnect based on quasi-coaxial signal transition: (a) return loss and (b) insertion loss.

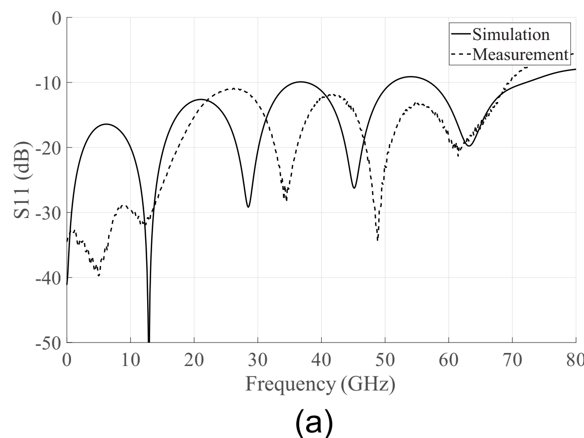

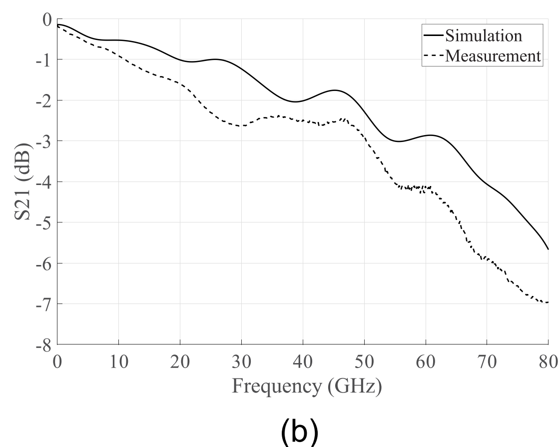

Figure 16. Measurement and simulation results of chip-to-package-to-PCB interconnect: (a) return loss and (b) insertion loss.

https://doi.org/10.1017/S1759078724000266 Published online by Cambridge University Press

The results for the back-to-back structure of the quasi-coaxial signal transition (Design A), are presented in Fig. 15. The simulation and measurement results agree very well. In both cases, the reflection coefficient is approximately equal to, or below, −10 dB, up to 103 GHz. The insertion loss of the back-to-back structure is less than or equal to 2 dB up to 80 GHz. Taking into consideration, there is 0.33 dB loss from the 2.5 mm CPW line on the PCB, and the 0.41 dB loss from the 1.65 mm long CPW line on the eWLB package (refer to Fig. 9), at 80 GHz. This results in an insertion loss of approximately 0.63 dB per quasi-coaxial transition at 80 GHz. It can similarly be determined that the loss per transition at 100 GHz is only 2.2 dB. The differences between the measurement and the simulation can be attributed to the manufacturing tolerances of the PCB substrate which is structured using laser ablation. It has been determined that the gaps between signal and ground lines of the CPW line are especially sensitive to manufacturing tolerances. Gap sizes can vary by up to $\pm 8\,\mu$m, which can have a significant influence on the impedance of the CPW line. Due to the manual assembly, it is also possible that the BGA height, and the antenna-to-reflector distance, can vary by up to 30 μm [11]. The insertion loss of quasi-coaxial signal transition can vary by approximately 0.4 dB, for a height difference of 30 μm (at 100 GHz).

There is an increase in the radiation loss above 85 GHz. There is finite spacing between the outer solder balls that constitute the outer conductor of the coax interconnect and at low frequencies, the spacing is electrically small compared to the operating wavelength so that interconnect functions as a coaxial transmission line, supporting a quasi-TEM mode. When the frequency increases, i.e. at 85 GHz and above, the spacing between the solder balls can no longer be ignored and the TEM mode becomes distorted. This distorted mode and the accompanying increase in radiation loss, causes the sudden increase in insertion loss. The distances between the solder balls are stipulated by the eWLB design rules.

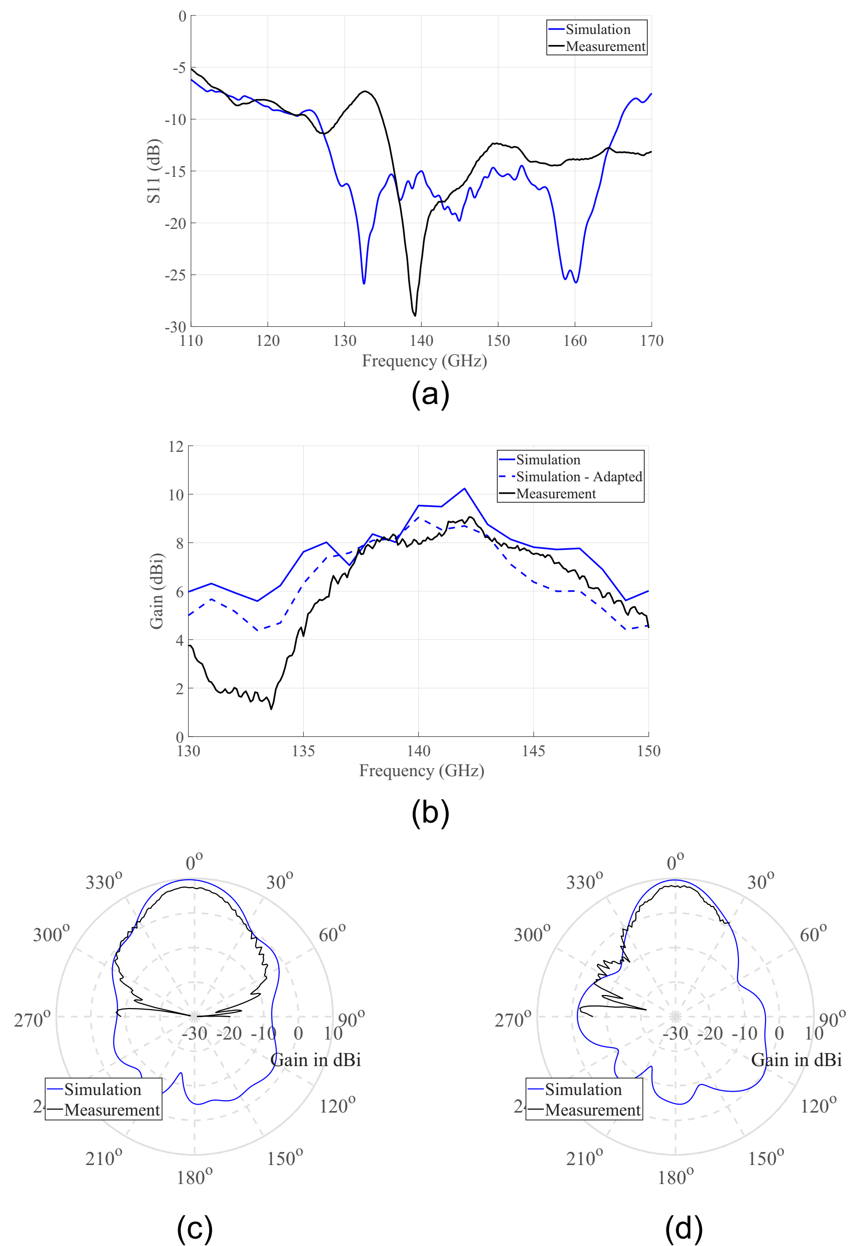

Figure 17. Measurement and simulation results of eSRR antenna: (a) reflection coefficient; (b) realized gain; (c) E-plane pattern; and (d) H-plane pattern.

https://doi.org/10.1017/S1759078724000266 Published online by Cambridge University Press

A complete structure of the chip-to-package-to-PCB chain, utilizing the quasi-coaxial signal transition, is also demonstrated here. The simulation and measurement results can be seen in Fig. 16. Once more, the simulation and measurement results correspond well. The measured reflection coefficient is equal or below −10 dB up to 70 GHz. The variation in the simulation and measurement results can be attributed to the reasons discussed above.

eSRR antenna

In this section, the simulated and measured gain, far-field pattern and return loss results are presented for the differential SRR-based antenna, in Fig. 17(a–d). Figure 17(a) shows simulated and measured reflection coefficients of the eSRR antenna. The simulated reflection coefficient is below −10 dB from 126.6 to 166 GHz, while the measured reflection coefficient is less than −10 dB from 135 to 170 GHz. That results in a relative bandwidth of 26.9% and 22.9%, for simulation and measurement, respectively. The resonances in the measured reflection coefficient appear to have shifted slightly higher, by 6.4 GHz, compared to the simulated reflection coefficient. The measured reflection coefficient rises slightly above −10 dB, to −7.3 dB, from 129 to 135 GHz.

The simulated peak gain is 10.2 dBi and the measured peak gain is 9.1 dBi – refer to Fig. 17(b). Various factors contribute to the difference between the measured and simulated gain results. Firstly, it was determined that the substrate height influences the gain of the antenna. The original design assumed a substrate thickness of 508 μm, which is a standard sheet thickness. However, in reality, when measured, it was determined that the substrate was actually 480 μm in thickness. This 30 μm difference in the substrate thickness causes an overall reduction in the gain across the 130–150 GHz frequency range and a reduction of approximately 0.4 dB in the peak gain. Secondly, it is important to note that it is required to place the antenna on a Rohacell 31 HF-based supporting foam (at 26.5 GHz, $\epsilon_r \approx 1.04$ and tan$\delta \approx 0.011$) on the antenna-under-test (AUT) holder, as the direction of radiation and the probe are in opposite directions. For further details on the calibration and measurement procedures of eWLB antennas, see [11]. The Rohacell supporting foam is therefore positioned directly between the AUT and the receiver on the measurement setup. Through simulation it is determined that the Rohacell supporting foam reduces the peak gain by approximately an additional 0.8 dB. Furthermore, measurements of the bond wires after manufacturing indicated that the loop profile of the wire bonds can differ from the simulation in terms of loop height, loop profile and the tail length. The balun performance is strongly dependent on the bond wire construction [12]. As aforementioned, the BGA height, and the antenna-to-reflector distance, can vary by up to 30 μm [11] – this will in turn influence the radiation patterns; the peak gain could vary with up to approximately 0.6 dB. Several facets of the measurement procedure explained in [11] influences the measured results, such as the probe placement, the calibration procedure, the AUT alignment and the loss of the Rohacell holder at D-band frequencies. Lastly, manufacturing tolerances in the horn cavity will also have an influence on the antenna's performance. In the final manufactured prototype, the slope of the horn reflector was measured to be between 17° and 19°, and the horn depth varied between 260 and 275 μm.

The substrate height was changed to 480 μm and the Rohacell supporting foam was included in the simulation model for the eSRR antenna with the horn-shaped reflector – the simulated gain for the adapted model is also shown in Fig. 17(b). When taking these changes into account, the simulated and measured gain agrees well overall. The difference around 132 GHz can be traced back to the mismatch in the return loss around the same frequency.

The E- and H-plane radiation patterns are shown in Fig. 17(c, d). Apart for the difference in gain, as discussed earlier, the patterns agree well between measurement and simulation.

Conclusion

An SiP for a wideband digital radar, in D-band, requires broadband, high-gain antennas combined with broadband

Table 2. BGA-based quasi-coaxial interconnects

Ref.	Bandwidth ($S11 \leq -10$ dB)	Insertion loss
[15]	DC – 60 GHz	3 dB @ 60 GHz
		For back-to-back hybrid model
[16]	DC – 35 GHz	0.4 dB @ 35 GHz
		For simulated transition
[17]	7–13 GHz	0.2 dB for 7–13 GHz
	($S11 < -20$ dB)	Measured per transition
[18]	DC – 20 GHz	5 dB @ 20 GHz
		For measured back-to-back structure
[19]	DC – 70 GHz	5 dB @ 70 GHz
		For measured back-to-back structure
[20]	DC – 97 GHz	3.4 dB @ 97 GHz
		Measured per transition
[21]	50–70 GHz	0.3 dB for 50–70 GHz
	($S11 < -20$ dB)	For simulated transition
This work	DC – 103 GHz	0.6 dB @ 80 GHz up to
		2.2 dB @ 100 GHz
		Measured per transition

Table 3. Summary of eWLB antennas above 100 GHz

Antenna	Frequency (GHz)	Relative bandwidth ($S11 \leq -10$ dB)	Peak gain (dBi)
Single-ended			
Bow-tie slot [10]	200–300	40%	4.2
Corner-fed patch [11]	115–162	34%	6
RSRR [13]	129–159	20.8%	6.4
Differential			
Bow-tie [10]	90–140	43.5%	5.8
Bow-tie [12]	130–150	14.3%	6.3
Dipole [12]	128–158	21%	7.1
Rhombic [12]	123–170	32.1%	8.1
SSRR [14]	126–170	29.7%	8.8
eSRR (this work)	127–166	26.9%	10.2

https://doi.org/10.1017/S1759078724000266 Published online by Cambridge University Press

chip-to-package and package-to-PCB interconnects. The contribution of this paper is twofold. Firstly, a wideband, low-loss quasi-coaxial signal transition is realized for the first time in eWLB technology. It was determined that the insertion loss per transition was less than 0.63 dB up to 80 GHz, and less than 2.2 dB up to 100 GHz. A chip-to-package interconnect is also demonstrated, with an on-chip microstrip transmission line in 22 nm FDSOI CMOS technology. The quasi-coaxial signal transition is combined with the chip-to-package transition to demonstrate its functionality and applicability for integration with MMICs for wide-band SiP applications in eWLB technology. In comparison with contemporary works presented in Table 2 the quasi-coaxial transition has several advantages – it is realized in commercially available technology; it exhibits very low loss up to 80 GHz; and it has the largest impedance bandwidth of the BGA-based quasi-coaxial signal transition without requiring specialized manufacturing technology.

Secondly, a modified reflector concept and a novel eSRR-based antenna were demonstrated. Prior publications of antennas realized in eWLB technology made use of a planar reflector realized on the PCB substrate. However, as the planar reflector is typically only a distance of 0.1λ from the antenna (at 140 GHz), it is inefficient in utilizing constructive interference, due the reflector, to improve the antenna gain. In the modified reflector concept, the reflector is placed approximately 0.25λ from the antenna, by micromachining a horn-shaped cavity in the alumina substrate and remetallizing the cavity through AJ-printing. The concept increases the antenna gain, with an improvement of 2.3 dB in the peak gain for the antenna with the horn-shaped reflector, in comparison with the antenna with the planar reflector. A significant improvement is especially noticeable at the higher frequencies – an improvement of up to 5.3 dB can be seen around 149 GHz. The simulated peak gain is 10.2 dBi and the measured peak gain is 9.1 dBi. Table 3 compares antennas realized in eWLB technology for frequencies above 100 GHz in order of ascending peak gain. The AiP with the horn-shaped reflector presented here, surpasses [14] as the single antenna element with the highest gain, in eWLB technology, above 100 GHz.

Acknowledgements. The authors would like to thank Christian Geissler and Vadim Issakov from Infineon AG for their support, and Andreas Lipp and Thorsten Fux from the IHE for their assistance.

Funding statement. This work is financially supported by the Federal Ministry of Education and Research (BMBF), Germany under the project “ForMikro-REGGAE” (16ES1061).

Competing interests. None declared.

References

1. **Kueppers S, Jaeschke T, Pohl N and Barowski J** (2022) Versatile 126–182 GHz UWB D-band FMCW radar for industrial and scientific applications. *IEEE Sensors Letters* **6**(1), 1–4.
2. **Probst F, Engelmann A, Hetterle P, Issakov V, Weigel R and Dietz M** (2022) A 15-gb/s pmcw radar prbs-generator for mimo and joint radar-communication systems. In *2022 Asia-Pacific Microwave Conference (APMC)*, 288–290.
3. **Engelmann A, Probst F, Hetterle P, Weigel R and Dietz M** (2022) A low-voltage broadband d-band bpsk modulator for a pmcw radar transmitter in 22 nm fdsoi. In *2022 Asia-Pacific Microwave Conference (APMC)*, 366–368.
4. **Hügler P, Geiger M and Waldschmidt C** (2016) RCS measurements of a human hand for radar-based gesture recognition at E-band. In *2016 German Microwave Conf. (GeMiC)*, 259–262.
5. **de Oliveira LG, Nuss B, Alabd MB, Diewald A, Pauli M and Zwick T** (2022) Joint radar-communication systems: modulation schemes and system design. *IEEE Transactions on Microwave Theory and Techniques* **70**(3), 1521–1551.
6. **Hagelauer A, Wojnowski M, Pressel K, Weigel R and Kissinger D** (2018) Integrated systems-in-package: heterogeneous integration of millimeter-wave active circuits and passives in fan-out wafer-level packaging technologies. *IEEE Microwave Magazine* **19**(1), 48–56.
7. **Beck C, Ng HJ, Agethen R, PourMousavi M, Forstner HP, Wojnowski M, Pressel K, Weigel R, Hagelauer A and Kissinger D** (2016) Industrial mmWave radar sensor in embedded wafer-level BGA packaging technology. *IEEE Sensors Journal* **16**(17), 6566–6578.
8. **Wojnowski M, Wagner C, Lachner R, Böck J, Sommer G and Pressel K** (2012) A 77-GHz SiGe single-chip four-channel transceiver module with integrated antennas in embedded wafer-level BGA package. In *2012 IEEE 62nd Electronic Components and Technology Conference*, 1027–1032.
9. **Hamidipour A, Fischer A, Maurer L and Stelzer A** (2012) A rhombic antenna array solution in eWLB package for millimeter-wave applications. In *2012 42nd European Microwave Conference*, 205–208.
10. **Ahmed F, Furqan M and Stelzer A** (2018) 120-GHz and 240-GHz broadband bow-tie antennas in eWLB package for high resolution radar applications. In *2018 48th Eur. Microwave Conf. (EuMC)*, 1109–1112.
11. **Bhutani A, Bekker E, de Oliveira LG, Pauli M and Zwick T** (2021) 140 GHz broadband antenna in embedded wafer-level ball grid array technology. In *2021 15th Eur. Conf. Antennas and Propagation (EuCAP)*, 1–5.
12. **Bhutani A, Bekker E, Li T, de Oliveira LG and Zwick T** (2022) 140 GHz differential antennas in embedded wafer-level ball grid array technology. In *2021 51st Eur. Microw. Conf. (EuMC)*, 881–884.
13. **Bekker E, Bhutani A, de Oliveira LG, Antes T and Zwick T** (2022) Broadband split ring resonator-based antennas at 140 GHz in embedded wafer level ball grid array technology. In *2022 International Workshop on Antenna Technology (iWAT)*, 60–63.
14. **Bekker E, Bhutani A, de Oliveira LG, Antes T and Zwick T** (2022) Differential split-ring resonator-based antenna at 140 GHz in embedded wafer level ball grid array technology. In *2022 52nd European Microwave Conference (EuMC)*, 528–531.
15. **Shao Y, Li X-C and Mao J-F** (2018) A broadband transition from substrate integrated coaxial line to BGA. In *2018 International Conference on Microwave and Millimeter Wave Technology (ICMMT)*, 1–3.
16. **Lu Q, Liu Y, Qiao Z, Liu L and Gao L** (2020) A study of a low-loss and ultra-wide band transmission structure through BGA based on HTCC technology. In *2020 7th International Conference on Information Science and Control Engineering (ICISCE)*, 144–147.
17. **Ling T, Zheng Y and Cui W** (2020) a study on subarray microwave boards interconnected by BGA. In *2020 International Conference on Microwave and Millimeter Wave Technology (ICMMT)*, 1–3.
18. **Zhang YZ, Wei W, Yong W, Biao S, XingWen Z, Jun X and Xing FX** (2021) Design of a broadband HTCC SiP packaging module. In *2021 International Conference on Microwave and Millimeter Wave Technology (ICMMT)*, 1–3.
19. **Yoshida S, Tanifuji S, Kameda S, Suematsu N, Takagi T and Tsubouchi K** (2010) Copper balls interconnection technology for 60 GHz band 3-D system-in-package modules. In *2010 Asia-Pacific Microwave Conference*, 904–907.
20. **Yoshida S and Nishikawa K** (2020) Experimental verification of excavated structure on multi-layered substrates for millimeter-wave signal vertical transition using copper balls. *IEEE Access* **8**, 2362–2372.
21. **Jafarlou S, Rashidian A and Tazlauanu M** (2017) Wideband LTCC transitions of flip-chip to waveguides/connectors for a highly dense phased array system-in-package at 60 GHz. In *2017 IEEE MTT-S International Microwave Symposium (IMS)*, 1753–1755.
22. **Pozar DM** (2021) *Microwave Engineering*. John Wiley & Sons, 130–131.
23. **Wojnowski M, Lachner R, Böck J, Wagner C, Starzer F, Sommer G, Pressel K and Weigel R** (2011) Embedded wafer level ball grid array (eWLB) technology for millimeter-wave applications. In *2011 IEEE 13th Electronics Packaging Technology Conference*, 423–429.

https://doi.org/10.1017/S1759078724000266 Published online by Cambridge University Press

24. **Eisenstadt WR and Eo Y** (1992) S-parameter-based IC interconnect transmission line characterization. *IEEE Transactions on Components, Hybrids, and Manufacturing Technology* **15**(4), 483–490.
25. **Padilla WJ, Aronsson MT, Highstrete C, Lee M, Taylor AJ and Averitt RD** (2006) Novel electrically resonant terahertz metamaterials. In *Photonic Metamaterials: From Random to Periodic*. Optical Society of America.
26. **Chen H-T, O'Hara JF, Taylor AJ, Averitt RD, Highstrete C, Lee M and Padilla WJ** (2007) Complementary planar terahertz metamaterials. *Optics Express* **15**(3), 1084–1095.
27. **Beer S and Zwick T** (2010) Probe based radiation pattern measurements for highly integrated millimeter-wave antennas. In *Proc. of the Fourth Eur. Conf. on Antennas and Propagation*, 1–5.
28. **Secor EB** (2018) Principles of aerosol jet printing. *Flexible and Printed Electronics* **3**(3), 035002.

Elizabeth Bekker received the B.Eng. and M.Eng. degrees in electronic engineering, both with distinction, from the University of Pretoria, Pretoria, South Africa, in 2017 and 2019, respectively. Since 2020, she is pursuing a doctorate (Ph.D.E.E.) degree at the Institute of Radio Frequency Engineering and Electronics (IHE) at the Karlsruhe Institute of Technology, Karlsruhe, Germany. Her work focuses on antennas and packaging solutions for radar and communication applications at millimeter-wave frequencies. She received the iWAT Best Paper Award and the EuMC Best Paper Award, both in 2022.

Georg Gramlich graduated from the Karlsruhe Institute of Technology (KIT) in electrical engineering, with distinction, and also received the diplôme d'Ingénieur from the Grenoble Institute of Technology (INP). After finishing his studies, he started working as a research associate at KIT, where he is currently pursuing his doctorate (Ph.D.E.E.) at the Institute of Radio Frequency Engineering and Electronics (IHE). His research is on digital manufacturing for RF electronics, with a focus on novel packaging solutions. He specializes in small-scale aerosol jet printing and accompanying technologies, including photonic sintering and laser machining.

Luca Valenziano received his master's degree in electrical engineering from the University of Applied Sciences Karlsruhe (HKA), Karlsruhe, Germany, in 2022. He is currently working as a research associate and pursuing a doctorate (Ph.D.E.E.) degree at the Institute of Radio Frequency Engineering and Electronics (IHE), Karlsruher Institute of Technology. His main research interests focus on concepts for millimeter wave (mmW) packaging and ultra-broadband packaging of electro-optical systems.

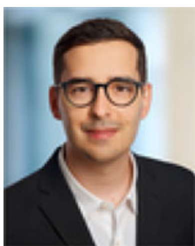

Lucas Giroto de Oliveira received the B.Sc. and M.Sc. degrees in electrical engineering, with a major in electronic systems, from the Federal University of Juiz de Fora (UFJF), Brazil, in 2017 and 2019, respectively. He is currently pursuing the Dr.-Ing. (Ph.D.E.E.) degree at the Institute of Radio Frequency Engineering and Electronics (IHE) of the Karlsruhe Institute of Technology (KIT), Germany. His research interests are in the areas of system design, signal processing, digital communication, and their applications to integrated radar sensing and communication systems and networks.

Theresa Antes received the B.Sc. and M.Sc. degrees in electrical engineering and information technology from the Karlsruhe Institute of Technology (KIT), Karlsruhe, Germany, in 2018 and 2020, respectively, where she is currently pursuing the Ph.D. degree in electrical engineering (EE) at the Institute of Radio Frequency Engineering and Electronics (IHE). Her main research interests include signal processing, high-accuracy radar systems, and radar-based gesture recognition.

Thomas Zwick obtained the Dipl.-Ing. (M.Sc.) and Dr.-Ing. (Ph.D.E.E.) degrees from the Universität Karlsruhe (TH), Germany, in 1994 and 1999, respectively. In October 2007, he became a full professor with the Karlsruhe Institute of Technology (KIT), Germany. He is currently the director of the Institute of Radio Frequency Engineering and Electronics (IHE), at KIT. His research topics include wave propagation, stochastic channel modeling, channel measurement techniques, material measurements, microwave techniques, millimeter-wave antenna design, wireless communication, and radar system design.

Akanksha Bhutani obtained the M.Sc. in Electrical Engineering and Information Technology and Dr.-Ing. (Ph.D.E.E.) degrees from Karlsruhe Institute of Technology (KIT), Germany, in 2012 and 2019, respectively. She worked as a research associate at the Institute of Radio Frequency Engineering and Electronics (IHE) in KIT from 2012 to 2019 and is currently leading the Antennas and Packaging research group at the IHE. Her research focuses on Terahertz Antennas and Package for radar and wireless communication. Bhutani has received the "Carl Freundenberg Prize" and the "Südwestmetall Advancement Award" for her dissertation titled "Low Temperature Co-fired Ceramics for System-in-Package Applications at 122 GHz". She has also received the IEEE Microwave Magazine Best Paper Award in 2019, EuMC Best Paper Award in 2019 and 2022, and is the author or co-author of over 40 research papers. Currently, Bhutani is serving as the Operations Director of the EuMW 2023 in Berlin.

https://doi.org/10.1017/S1759078724000266 Published online by Cambridge University Press